Available online at www.sciencedirect.com

ScienceDirect

International Journal of Solids and Structures 44 (2007) 2109–2129

INTERNATIONAL JOURNAL OF SOLIDS and STRUCTURES

www.elsevier.com/locate/ijsolstr

Stress analysis of a layered elastic solid in contact with a rough surface exhibiting fractal behavior

K. Komvopoulos *, Z.-Q. Gong

Department of Mechanical Engineering, University of California, Berkeley, CA 94720, United States

Received 17 November 2005; received in revised form 21 February 2006
Available online 4 July 2006

Abstract

A contact stress analysis is presented for a layered elastic half-space in contact with a rough surface exhibiting self-affine (fractal) behavior. Relationships for the mean contact pressure versus representative strain and the real half-contact width versus elastic properties of the layer and the substrate, asperity radius, layer thickness, and truncated half-contact width were derived from finite element simulations of a layered medium compressed elastically by a rigid cylindrical asperity. These relationships were incorporated in a numerical algorithm that was used to obtain the contact pressure distributions and stresses generated by the asperity contacts formed at the interface of the layered medium and the fractal surface. Analytical solutions illustrate the significance of the elastic material properties, layer thickness, and surface topography (roughness) on global parameters such as normal load and real contact area. Results for the contact pressure distribution and the surface and subsurface stresses provide insight into the initiation of yielding and the tendency for cracking in the layered medium. It is shown that cracking at the surface and the layer/substrate interface is more likely to occur in the case of a stiff layer, whereas surface cracking is more prominent for a relatively compliant layer.

Keywords: Elastic contact; Layered media; Fractal surfaces; Stress analysis

1. Introduction

Since the pioneering contact analysis of elastic solids of revolution by Hertz (1882), contact deformation of homogeneous bodies with smooth surfaces has been the subject of a voluminous literature including both analytical and numerical studies. Despite important insight into contact mechanics derived from early studies, real contact interfaces possess rough topographies. Hence, the contact stress and strain fields obtained for ideally smooth and homogeneous bodies deviate significantly from those of real contact interfaces of layered media. One of the earliest contact analyses of layered elastic media is attributed to Burmister (1945), who developed an elasticity theory for axisymmetric contacts and obtained solutions for the contact pressure distribution. Aleksandrov et al. (1966) presented a mathematical formulation of three-dimensional contact of a frictionless

* Corresponding author. Tel.: +1 510 642 2563; fax: +1 510 643 5599.
E-mail address: kyriakos@me.berkeley.edu (K. Komvopoulos).

0020-7683/$ - see front matter
doi:10.1016/j.ijsolstr.2006.06.043

stamp and an elastic layer supported by a rigid substrate, which was limited to a layer thickness less than the size of the contact region. Pao et al. (1971) determined the maximum contact pressure on an elastic layer indented by a cylinder for the extreme cases of frictionless and rigid layer/substrate interfaces. Gupta and Walowit (1974) analyzed contact of a cylindrical indenter and a layered half-space using an integral equation approach and evaluated the dependence of the contact pressure on the stiffness of the cylinder, layer, and substrate materials.

Contact analysis of elastic–plastic layered media attracted significant attention in later years as a result of the development of efficient numerical methods for complex contact analysis. Van der Zwaag and Field (1982) used the finite element method (FEM) to examine the effect of a thin and hard layer on the stresses produced in a layered medium indented by a rigid sphere. While the stiff layer significantly decreased the tensile stresses in the substrate (especially in the vicinity of the contact edge), it also intensified the shear stress at the layer/substrate interface and the surface tensile stress at the contact edge. A similar result was reported by Komvopoulos (1988, 1989), who performed plane-strain FEM analyses and obtained solutions for the subsurface stresses and strains in terms of the layer thickness, friction coefficient at the contact region, and elastic–plastic properties of the layer and the substrate materials. Bhattacharya and Nix (1988) analyzed indentation of a layered medium by a rigid cone with the FEM and examined the effects of the elastic–plastic properties of the layer and the substrate on the effective hardness of the layered medium. Kral and Komvopoulos (1996) presented a three-dimensional FEM analysis of a rigid sphere sliding on an elastic–plastic layered medium that demonstrated the significance of the layer material properties, contact friction, and normal load on the contact pressure distribution and subsurface stresses.

The previous analytical and numerical studies involved ideally smooth contact interfaces. However, in view of the scale-dependence roughness of real surfaces, actual contact occurs at surface summits referred to as asperities. Therefore, the results reported for smooth surfaces are not applicable at the microscale where multi-scale roughness greatly affects the local deformation behavior. Contact analysis of real (rough) surfaces is cumbersome due to the randomness of the surface topography. To circumvent this difficulty, in earlier studies the surface topography was represented by a periodic waviness. For instance, Nowell and Hills (1989) used an iterative method to analyze compression of an elastic cylinder with a wavy surface by a rigid and smooth cylinder and noted the occurrence of local stress maxima below the asperity contacts. Ioannides and Kuijpers (1986) carried out a numerical contact analysis that showed a significant roughness effect on the subsurface stresses at the asperity scale. Similar results were obtained by Komvopoulos and Choi (1992), who used an FEM model to study asperity interaction in terms of the radius and lateral spacing of the spherical asperities of a rigid surface indenting an elastic half-space.

The important role of the surface roughness in contact deformation demonstrated in earlier studies motivated the development of more sophisticated surface models in contemporary contact mechanics analyses. Chang et al. (1987) represented the surface roughness by asperities of constant radius of curvature that followed a Gaussian height distribution and used an elastic–plastic asperity model which accounted for volume conservation during plastic flow to obtain analytical solutions for the mean surface separation and the contact area. In elastic contact models developed by Bush et al. (1975, 1979), Gibson (1982), and McCool (1986), the asperities were modeled by elliptical paraboloids, resulting in randomly oriented elliptical contacts at the interface. While these statistical models provided simple relationships for the normal load in terms of the contact area, the effects of multi-scale roughness and asperity interaction were not considered in the former studies.

To overcome the dependence of traditional roughness parameters on the sample size, instrument resolution, and experimental filter, the surface morphology was described by fractal geometry (Mandelbrot, 1983). Analytical and numerical contact analyses of rough surfaces possessing self-affine (fractal) topographies have elucidated the effect of surface roughness on the real contact area and the normal load (Yan and Komvopoulos, 1998; Ciavarella et al., 2000; Komvopoulos and Ye, 2001; Persson, 2001; Persson et al., 2002; Hyun et al., 2004), temperature rise at the contact interface due to frictional heating (Wang and Komvopoulos, 1994a,b), and electrical conductance across rough contact interfaces (Barber, 2003; Kogut and Komvopoulos, 2003a; Ciavarella and Leoci, 2006), including the effects of surface roughness (constriction resistance) and electron tunneling across an insulating thin film at the contact interface (Kogut and Komvopoulos, 2003b, 2004). However, studies dealing with the subsurface stresses and strains at the asperity scale are sparse, presumably due to the highly complex and computationally intensive analysis of interacting elastic–plastic solids with

random surface topographies. One of the first comprehensive FEM analysis of elastic–plastic contact to deal with real surface topographies (such as those of magnetic recording heads and thin-film rigid disks) exhibiting fractal behavior is attributed to Komvopoulos and Ye (2002). More recently, Gong and Komvopoulos (2005) presented a thermomechanical analysis of a rough (fractal) surface sliding on a semi-infinite homogeneous elastic medium that included the coupled effects of thermal and mechanical deformation.

Although the FEM is an effective technique for calculating the stresses and strains in contacting solids with rough surfaces, the excessive number of finite elements needed to accurately model contact of surfaces exhibiting multi-scale roughness prohibits the use of a sufficiently large and refined mesh. Therefore, the main objective of this study was to develop a comprehensive analysis of layered elastic solids in contact with a rough surface characterized by fractal geometry. To accomplish this objective, plane-strain FEM simulations of a single asperity indenting a layered elastic medium were performed to obtain relationships for the mean contact pressure and the real half-contact width in terms of the asperity radius, truncated half-contact width, layer thickness, and elastic properties of the layer and the substrate. These relationships were incorporated in the contact stress analysis, and numerical solutions were obtained for the normalized contact load, real contact area, contact pressure, and subsurface stresses in terms of fractal parameters (surface roughness), coefficient of friction, layer thickness, and elastic properties of the layer and substrate materials. Numerical results provided insight into the tendency for yielding and cracking in the layered medium due to sliding against a fractal surface.

2. Surface characterization

As mentioned previously, surface topography parameters derived from traditional approaches depend on the sample length and instrument resolution. Fractal geometry enables unbiased surface description and maintains the self-affinity property of real surfaces over a wide range of length scales. Since the details of the surface topography description by fractal geometry can be found in previous publications (e.g., see Majumdar and Bhushan, 1990; Wang and Komvopoulos, 1994a; Yan and Komvopoulos, 1998), only the function $z(x)$ of the two-dimensional fractal surface used in the analysis will be presented here for brevity. For consistency, $z(x)$ can be written as (Wang and Komvopoulos, 1994a)

$$z(x) = L\left(\frac{G}{L}\right)^{(D-1)} \sum_{n=0}^{n_{\max}} \frac{\cos(2\pi\gamma^n x/L)}{\gamma^{(2-D)n}}, \tag{1}$$

where L is the fractal sample length, G is a frequency independent parameter referred to as the fractal roughness, D ($1 < D < 2$) is the fractal dimension that controls the contribution of high- and low-frequency components in the surface function (e.g., high D values are indicative of smooth surfaces), γ ($\gamma > 1$) is a scaling parameter with a typical value of 1.5 (Komvopoulos and Yan, 1997), and n is a frequency index with an upper limit given by $n_{\max} = \text{int}[\log(L/L_s)/\log\gamma]$, where int[...] denotes the integer part of the number in the brackets, and L_s is the cutoff length. G and D can be determined from a log–log plot of the structure function of $z(x)$ versus wavelength (Komvopoulos, 2000). The cutoff length and the fractal sample length define, respectively, the smallest and the largest wavelengths in the surface profile. Thus, Eq. (1) exhibits a scale-invariant (fractal) behavior within a finite range of wavelengths, outside of which the surface topography can be represented by a deterministic function (Wang and Komvopoulos, 1994b).

3. Contact analysis

The two-dimensional plane-strain problem of a rigid, rough (fractal) surface sliding against an elastic layered medium is shown schematically in Fig. 1. Coulomb friction is assumed between the rough surface and the surface of the layered medium. Therefore, the layered medium is subjected to distributed normal and tangential tractions, producing a total normal load P and a total tangential (friction) force $F = \mu P$, where μ is the coefficient of friction.

3.1. Constitutive relationships

To accurately determine the normal and friction forces at the asperity contacts, it is necessary to obtain first a contact stress–strain relationship and an expression for the real contact width in terms of the truncated

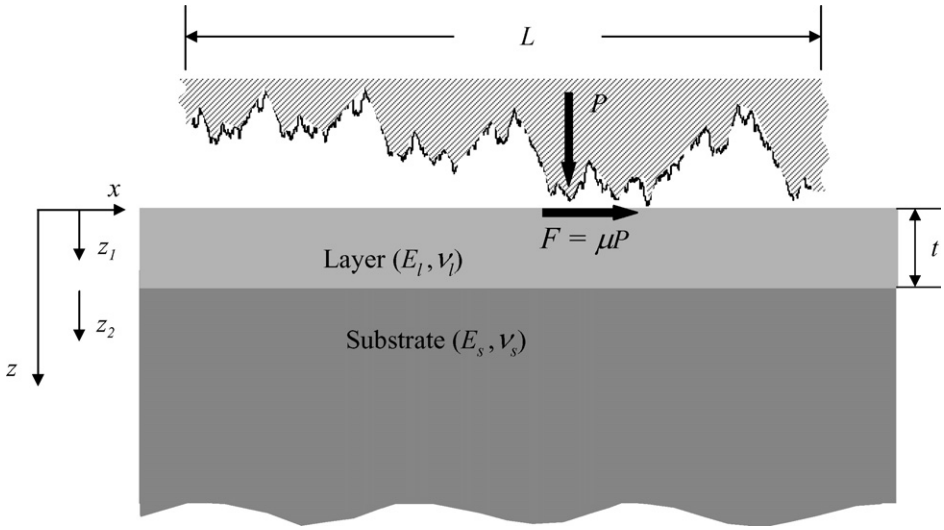

Fig. 1. Schematic representation of an elastic layered medium in contact with a rigid rough surface.

contact width, both derived for a single asperity in contact with a layered elastic medium. For this purpose, quasi-static indentation of a layered elastic medium by a rigid cylindrical asperity was analyzed with the FEM. Fig. 2 shows the mesh used in the FEM simulations, which consists of 6417, eight-node, isoparametric, quadrilateral elements, resulting in a total of 19,232 nodes. A 3×3 integration scheme was used in the isoparametric elements. A magnification of the refined mesh at the surface is shown on the left hand-side of Fig. 2. The horizontal and vertical dimensions of the mesh are equal to $2.4R$ and $3.1R$, respectively, where R is the radius of the rigid asperity. The nodes of the bottom boundary of the mesh were constrained against displacement in

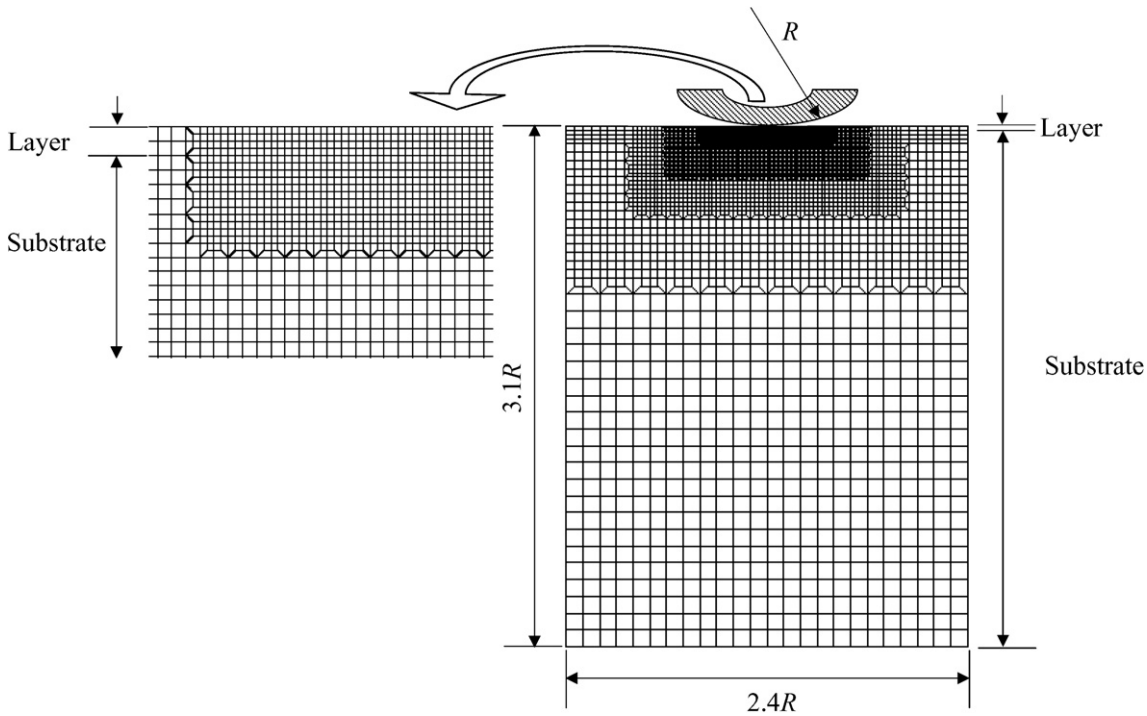

Fig. 2. Finite element discretization of an elastic layered medium. The refinement of the mesh at the surface is shown on the left-hand side.

the vertical direction, while the nodes of the left and right boundaries were constrained against displacement in the horizontal direction. The simulations were performed with the multi-purpose FEM code ABAQUS. An elastic modulus $E = 114$ GPa and Poisson ratio $v = 0.3$ were assigned to the substrate elements. To examine the effect of the layer stiffness on the mean contact pressure and the real contact width, the elastic modulus of the layer was varied so that $E_l/E_s = 8$, 4, 2, 1, 0.5, 0.25, and 0.125, where E_l and E_s are the elastic modulus of the layer and the substrate, respectively. Fig. 3 shows that the normalized mean contact pressure p_m/E_s varies linearly with the representative strain $E_e^* r/E_s R$, where r is the real half-contact width and E_e^* is the equivalent (effective) elastic modulus of the layered medium given by (King, 1987)

$$E_e^* = \left[\left(1 - e^{-\alpha t/r\sqrt{\pi}}\right)\frac{1-v_l^2}{E_l} + e^{-\alpha t/r\sqrt{\pi}}\frac{1-v_s^2}{E_s} + \frac{1-v_i^2}{E_i}\right]^{-1}, \tag{2}$$

where α is a geometric factor that depends on the indenter shape, t is the layer thickness, and subscripts l, s, and i refer to the layer, substrate, and indenter materials, respectively. The following relationship for the mean contact pressure was obtained after performing a least-square fit to the data shown in Fig. 3:

$$\frac{p_m}{E_s} = \frac{\pi}{8}\left(\frac{E_e^* r}{E_s R}\right). \tag{3}$$

Eqs. (2) and (3) represent general relationships for layered elastic solids. For the extreme cases of $t \to \infty$ and $t \to 0$, Eq. (3) becomes identical to the Hertzian solution of a half-space with layer and substrate elastic properties, respectively. For the special case of $E_l/E_s = 1$, Eq. (3) yields the mean contact pressure on a homogeneous half-space predicted by Hertz theory. For the extreme case of $E_l \ll E_s$, linearization of the exponential term in Eq. (2) and setting $\alpha = 2$ (King, 1987) gives

$$\frac{p_m}{E_s} \approx \frac{r^2 E_l}{2.9 t R(1-v_l^2)E_s}. \tag{4}$$

Eq. (4) is similar to the analytical solution of an elastic foundation model (Johnson, 1985). For the other extreme case of $E_l \gg E_s$, Eq. (3) yields infinite pressure because of the zero contact area resulting for a rigid cylinder loaded on a rigid layer on elastic foundation.

Fig. 4 shows the normalized real half-contact width r/R as a function of E_l/E_s and r'/R, where r' is the truncated half-contact width. As expected, the stiffer the layer, the smaller the half-contact width. From a least-square fit through the data shown in Fig. 4 (correlation factor = 0.9991), it was found that

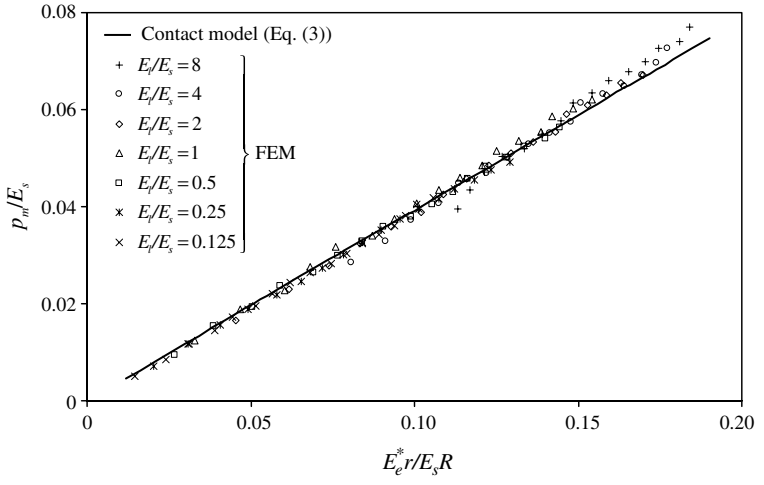

Fig. 3. Normalized mean contact pressure versus representative strain for an elastic layered medium with different layer-to-substrate elastic modulus ratio.

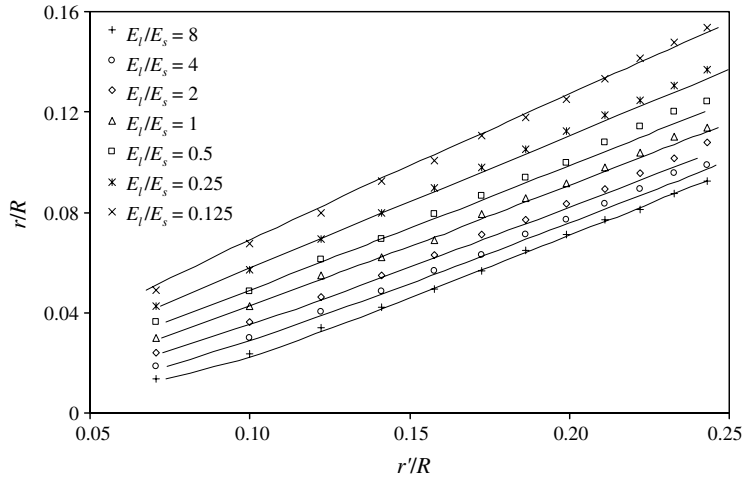

Fig. 4. Real half-contact width versus truncated half-contact width for an elastic layered medium with different layer-to-substrate elastic modulus ratio. (Symbols represent finite element results and solid lines are solutions obtained from Eq. (5).)

$$\frac{r'}{R} = \beta_1 \left(\frac{E_e^*}{E_s}\right)^{\beta_2} \left(\frac{r}{R}\right)^{\beta_3}, \tag{5}$$

where $\beta_1 = 1.7474$, $\beta_2 = 0.3943$, and $\beta_3 = 0.9189$. It is noted that the layer thickness is implicitly included in Eq. (5) through the effective elastic modulus E_e^* (Eq. (2)). Results obtained from Eq. (5) and FEM simulations for different values of E_l/E_s were found to be in good agreement.

3.2. Stress analysis

As the rough surface interferes with the layered medium, asperity contacts are established within the apparent contact area. There has been considerable debate in the literature of what constitutes an asperity. Ciavarella and Leoci (2006) reported that results based on the widely used definition of asperity (peak) as a local maximum of the surface profile, adopted from the classical contact model of Greenwood and Williamson (1966), are in disagreement with results for surfaces exhibiting multi-scale roughness. Recently, Greenwood and Wu (2001) acknowledged that the association of the peaks of a surface profile with the contact asperities does not have any physical significance and leads to questionable results for both the number and the radius of curvature of the asperities. It was argued that the earlier concept of Archard (1957) that topography consists of small spheres distributed on top of larger spheres and so on (a simple fractal-like model) should be used to correctly capture the mechanics of contacting asperities. The use of fractal geometry to describe the surface topography and the determination of the asperity contacts by an incremental truncation procedure does not require *a priori* definition of the asperities. In addition, because of the randomness of the fractal profile, a wide range of wavelengths can be included in the analysis for a given interference.

In the present study the total deformation force at the contact interface was obtained by numerical integration of the forces generated at individual asperity contacts over the entire contact interface. Asperity contacts were established by truncating the rough surface by a rigid plane for various interferences. For a truncated asperity of half-contact width r' (Fig. 5), the largest wavelength in the asperity waveform is equal to $2r'$. It is assumed that the asperity contact force is due to the deformation of an asperity represented by the base wavelength (Yan and Komvopoulos, 1998) with frequency index n_0 and cosine function z_0 given by

$$n_0 = \frac{\ln(L/2r')}{\ln \gamma} \tag{6}$$

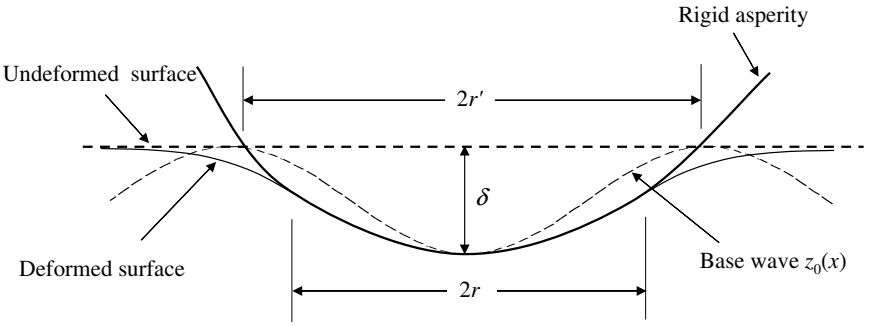

Fig. 5. Schematic illustration of contact between a rigid asperity of a rough surface and an elastic medium.

and

$$z_0(x) = G^{(D-1)}(2r')^{(2-D)}\cos\left(\frac{\pi x}{r'}\right). \tag{7}$$

The former approximation is consistent with earlier studies (Yan and Komvopoulos, 1998; Greenwood and Wu, 2001) where the deformation of a compressed asperity was determined by the large-scale geometry of the asperity. As shown in Fig. 5, the asperity interference δ is equal to the peak-to-valley amplitude of the cosine function z_0 (Eq. (7)); hence,

$$\delta = 2G^{(D-1)}(2r')^{(2-D)}. \tag{8}$$

Since the contact interface is modeled by a deformable surface compressed by rigid cylindrical asperities, the radius can be written as

$$R = \frac{(r')^2}{2\delta}. \tag{9}$$

In general, the asperity radius is much larger than the asperity height. Thus, Eq. (9) was obtained by approximating the cosine function of the asperity by a circular profile. Substituting Eq. (8) into Eq. (9) gives

$$R = \frac{(r')^D}{2^{(4-D)}G^{(D-1)}}. \tag{10}$$

In view of Eqs. (5) and (10), the truncated half-contact width can be expressed as

$$r' = \left[2^{(D-4)(1-\beta_3)}\beta_1\left(\frac{E_e^*}{E_s}\right)^{\beta_2}G^{(1-D)(1-\beta_3)}r^{\beta_3}\right]^{\frac{1}{1-D+D\beta_3}}. \tag{11}$$

Using Eq. (3), the elastic force at an asperity contact is

$$\Delta F_{df} = \frac{\pi G^{(D-1)}E_e^* r^2}{2^{(D-2)}(r')^D}. \tag{12}$$

Substituting Eq. (11) into Eq. (12) gives

$$\Delta F_{df} = 2^{(2+D-2D\beta_3)/(1-D+D\beta_3)}\pi G^{(D-1)}E_e^*\left[G^{(1-D)(1-\beta_3)}\beta_1\left(\frac{E_e^*}{E_s}\right)^{\beta_2}\right]^{\frac{-D}{1-D+D\beta_3}} r^{2-D\beta_3/(1-D+D\beta_3)}. \tag{13}$$

Because the equivalent elastic modulus (Eq. (2)) is a function of the real contact width, which is not known *a priori*, an iteration procedure was used to determine E_e^* and r in order to simultaneously satisfy Eqs. (2) and (5). The initial value of r was set equal to r'. Hence, the real contact width and corresponding equivalent elastic

modulus were determined at each asperity contact using the previous iteration procedure, and the associated elastic force was calculated from Eq. (13). Hence, the total contact force was obtained as

$$F_{\mathrm{df}} = \sum_{i=1}^{N} \Delta F_{\mathrm{df}}^{i}, \tag{14}$$

where $\Delta F_{\mathrm{df}}^{i}$ is the deformation force of the ith asperity contact and N is the number of the asperity contacts formed across the interface for a given interference.

Contact pressure distributions were determined from a numerical procedure in which the nodal contact pressure was proportional to the square root of the local interference. This proportionality relationship can be derived from the Hertzian contact pressure distribution, assuming very small interference compared to the indenter radius in order for linear elasticity to hold (Johnson, 1985). As shown in Fig. 6, a piecewise-linear distribution of the contact pressure was obtained by the superposition of overlapping triangular pressure elements (Johnson, 1985). The peak value of the jth triangular pressure element p_i^j at the ith asperity contact is given by

$$p_i^j = \frac{\sqrt{\delta_i^j}}{\sum_{j=1}^{M_i-1} \sqrt{\delta_i^j}} \frac{\Delta F_{\mathrm{df}}^{i}}{\xi}, \tag{15}$$

where δ_i^j is the local interference at the jth point, M_i is the total number of grid nodes in the ith asperity contact, and ξ is the grid size. Using a piecewise-linear distribution to approximate the contact pressure yielded continuous surface displacements. For fully developed sliding contact, it was assumed that the contact pressure profile was not affected by the shear traction, $q(x) = \mu p(x)$, which is a reasonable assumption for low-friction sliding.

The stresses in the layered medium were obtained by superposition of the stress fields generated by the triangular distributions of normal and tangential tractions at each asperity contact, using the approach of Gupta et al. (1973), and another superposition of the stress fields of all the asperity contacts forming at the interface. Referring to the coordinate system shown in Fig. 7, the stresses and the displacements in the layer are functions of x and z_1, while in the substrate they are functions of x and z_2. The stresses can be expressed in terms of an Airy stress function Φ that satisfies the biharmonic equation $\nabla^4 \Phi = 0$, which can be differentiated to obtain the stresses, i.e.,

$$\sigma_{zz} = \frac{\partial^2 \Phi}{\partial x^2}, \quad \sigma_{xx} = \frac{\partial^2 \Phi}{\partial z^2}, \quad \sigma_{zx} = -\frac{\partial^2 \Phi}{\partial z \partial x}. \tag{16}$$

The traction boundary conditions at the layer surface and the continuity of the displacements and tractions across the layer/substrate interface are expressed as

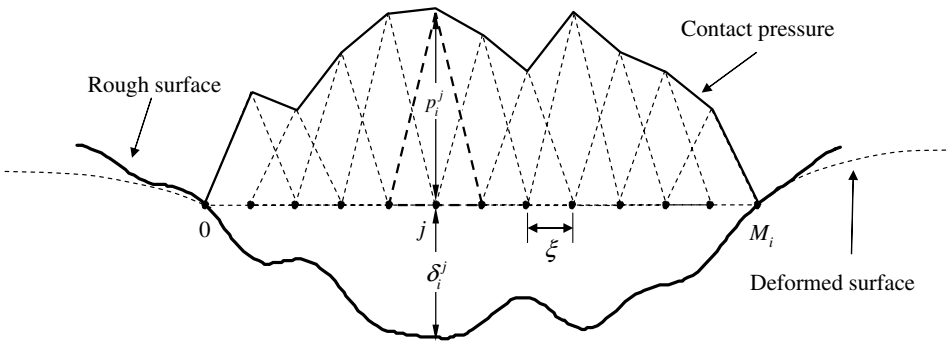

Fig. 6. Piecewise-linear contact pressure profile consisting of overlapping triangular pressure elements used in the numerical procedure.

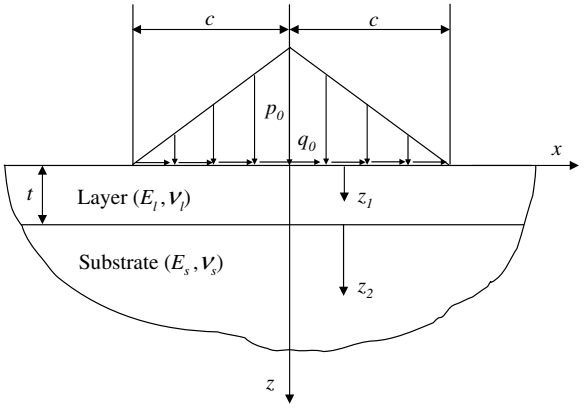

Fig. 7. Coordinate systems used in the analysis of a layered medium subjected to triangular distributions of normal and tangential tractions.

$$
\begin{aligned}
\sigma_{zz}^{(1)}(x,0) &= \begin{cases} -p_0(1-|x|/c) & |x| \leqslant c, \\ 0 & |x| > c, \end{cases} \\
\sigma_{xz}^{(1)}(x,0) &= \begin{cases} -q_0(1-|x|/c) & |x| \leqslant c, \\ 0 & |x| > c, \end{cases} \\
\sigma_{xz}^{(1)}(x,h) &= \sigma_{xz}^{(2)}(x,0), \\
\sigma_{zz}^{(1)}(x,h) &= \sigma_{zz}^{(2)}(x,0), \\
u^{(1)}(x,h) &= u^{(2)}(x,0), \\
w^{(1)}(x,h) &= w^{(2)}(x,0),
\end{aligned}
\tag{17}
$$

where superscripts 1 and 2 refer to the layer and the substrate and u and w denote displacements in the x and z directions, respectively. The solution was obtained by a Fourier transform of function Φ with respect to x, given by

$$
\overline{\Phi} = \int_{-\infty}^{+\infty} \Phi(x,z) \mathrm{e}^{\mathrm{i}\omega x} \, \mathrm{d}x. \tag{18}
$$

For function Φ to satisfy the biharmonic equation and yield finite stresses at infinity it should be of the form:

$$
\begin{aligned}
\overline{\Phi}^{(1)} &= (A_1 + B_1 z_1)\mathrm{e}^{-|\omega| z_1} + (C_1 + D_1 z_1)\mathrm{e}^{|\omega| z_1}, \\
\overline{\Phi}^{(2)} &= (A_2 + B_2 z_2)\mathrm{e}^{-|\omega| z_2},
\end{aligned}
\tag{19}
$$

where $\overline{\Phi}^{(1)}$ and $\overline{\Phi}^{(2)}$ are the solutions of $\overline{\Phi}$ in the layer and the substrate, respectively. The two boundary conditions and the four interfacial conditions comprise a set of six coupled equations, including the coefficients in Eq. (19) and the Fourier transforms of the surface traction distributions $p(x,z)$ and $q(x,z)$. Upon the determination of $\overline{\Phi}$, the stresses were calculated from Eqs. (16) by an inverse transformation of $\overline{\Phi}$.

Therefore, the stress at a point $A(x,z)$ in the layered medium can be written as

$$
\sigma(x,z) = \sum_{i=1}^{N} \sum_{j=1}^{M_i - 1} \sigma|_i^j(x,z), \tag{20}
$$

where $\sigma|_i^j$ indicates the stress due to the jth triangular distributions of the contact pressure and the tangential (friction) tractions at the ith contact spot.

4. Results and discussion

4.1. Validation of the contact algorithm

To validate the analytical model of the layered elastic medium, numerical results for a homogeneous elastic half-space ($E = 114$ GPa and $v = 0.3$) in contact with a rigid cylinder are contrasted with theoretical results (Johnson, 1985). Fig. 8(a) shows the normalized contact pressure distribution of the indented homogeneous half-space. The x coordinate was normalized by the half-contact width r_0 and the contact pressure p by the maximum contact pressure p_0. The good agreement between analytical and theoretical results confirms the validity of the model and the assumption that the local contact pressure is proportional to the square root of the corresponding interference. Fig. 8(b) shows the effect of the elastic modulus ratio on the pressure profile due to the indentation of a layered medium by a rigid cylinder. Similar with Fig. 8(a), the maximum contact pressure p_0 and corresponding half-contact width r_0 of the homogeneous half-space ($E_l/E_s = 1$) were used to normalize the contact pressure distributions and the x coordinate, respectively. As expected, higher contact pressure and smaller contact width were produced with stiffer layers ($E_l/E_s > 1$) and vise versa for compliant layers ($E_l/E_s < 1$). The contact pressure distributions do not resemble Hertzian profiles, especially for large differences in the elastic modulus of the layer and the substrate media. The contact pressure profiles shown in Fig. 8(b) are in good agreement with similar results obtained by King and O'Sullivan (1987).

The normalized subsurface stresses σ_{xx}, σ_{zz}, and τ_I (principal shear stress) along the axis of symmetry of a homogeneous half-space due to frictionless indentation ($\mu = 0$) and the normalized surface stresses σ_{xx}, σ_{zz}, and τ_{xz} due to sliding ($\mu = 0.5$) of a rigid cylinder are shown in Figs. 9(a) and (b), respectively. The symbols represent numerical results, while the curves are theoretical solutions (Johnson, 1985). The good agreement between numerical and analytical results demonstrates the accuracy of the algorithm and justifies the use of the piecewise-linear contact pressure distributions. Fig. 9(b) shows the development of a maximum surface tensile stress at the trailing edge of the contact region that was accurately predicted by the numerical algorithm.

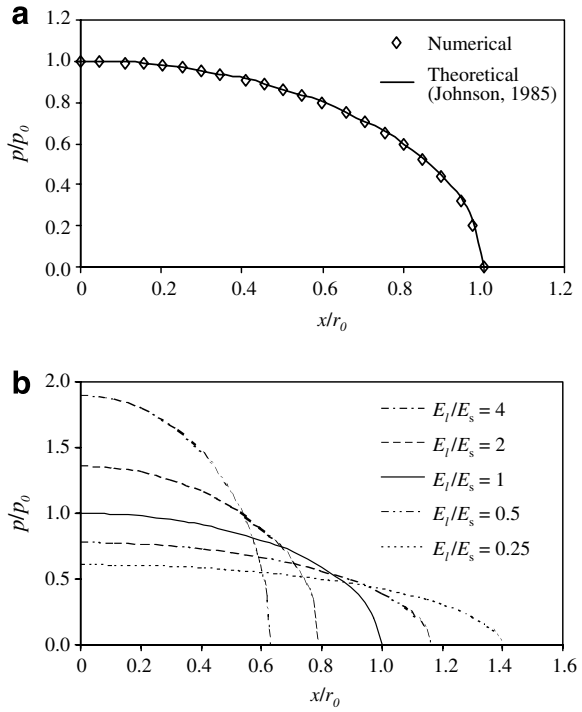

Fig. 8. Contact pressure distributions due to compression of (a) homogeneous and (b) layered medium by a rigid cylinder versus layer-to-substrate elastic modulus ratio.

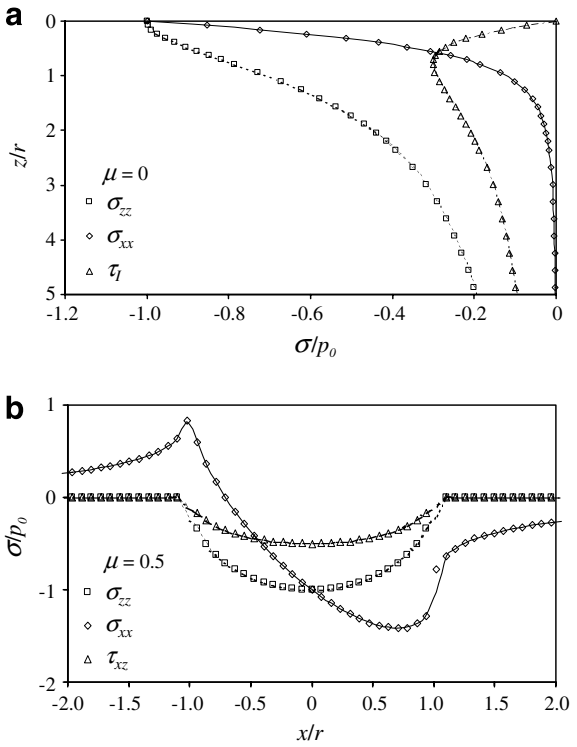

Fig. 9. (a) Subsurface stresses along the axis of symmetry and (b) surface stress distributions due to compression of a layered elastic medium by a rigid cylinder. (Symbols represent numerical results and curves indicate theoretical solutions (Johnson, 1985).)

The results shown in Figs. 8 and 9 indicate that the present analysis yields accurate solutions for the surface and subsurface stresses resulting from normal and tangential surface tractions.

4.2. Contact load and contact area

Results for the contact load and the contact area are presented first to elucidate the significance of the elastic properties of the layered medium, layer thickness, and surface topography (roughness) on global parameters. The effects of the coefficient of friction, layer thickness, and elastic properties on the pressure profile and the various stress components are discussed next. All the results presented hereafter are for $L = 5$ μm, $G = 9.46 \times 10^{-4}$ nm, $E_s = 114$ GPa, and $\nu_l = \nu_s = 0.3$.

The effect of the root-mean-square surface roughness σ, which increases with decreasing D, on the contact load and the real contact area can be interpreted in light of the results shown in Fig. 10 for $E_l/E_s = 2$. The figure shows that both the normalized contact load P/E_sA_a and the normalized real contact area A_r/A_a increase with the normalized maximum surface interference δ_{max}/t. Fig. 10(a) shows that the decrease of the surface roughness (i.e., increase of t/σ) produced high contact loads for large interferences and the opposite for small interferences. This is because only one or two asperity contacts were established for a small interference, and the rough surface ($t/\sigma = 0.23$) resulted in sharper contacting asperities that yielded higher contact loads. With the increase of δ_{max}/t, the smoother surface ($t/\sigma = 4.17$) generated more asperity contacts, producing higher contact loads due to the more pronounced increase of the real contact area compared to the other surface topographies. Fig. 10(b) shows that, for fixed δ_{max}/t, the real contact area increased significantly with the decease of the surface roughness (i.e., increase of t/σ).

Fig. 11 shows the dependence of the normalized contact load P/E_sA_a and the real contact area A_r/A_a on δ_{max}/σ and E_l/E_s for $t/\sigma = 1$ ($D = 1.44$). As expected, both the contact load and the real contact area increased with the maximum interference. For fixed δ_{max}/σ, the contact load increased and the contact area decreased

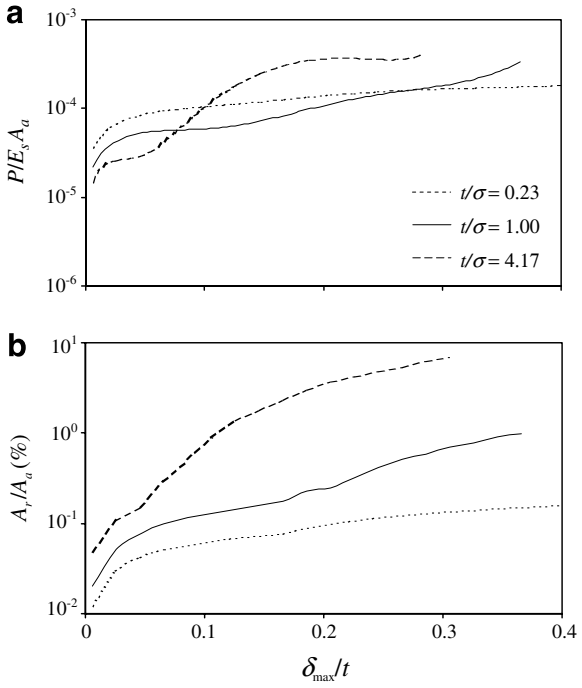

Fig. 10. Effect of surface roughness on (a) contact load and (b) real contact area versus maximum surface interference for a layered elastic medium indented by a rough surface ($E_l/E_s = 2$).

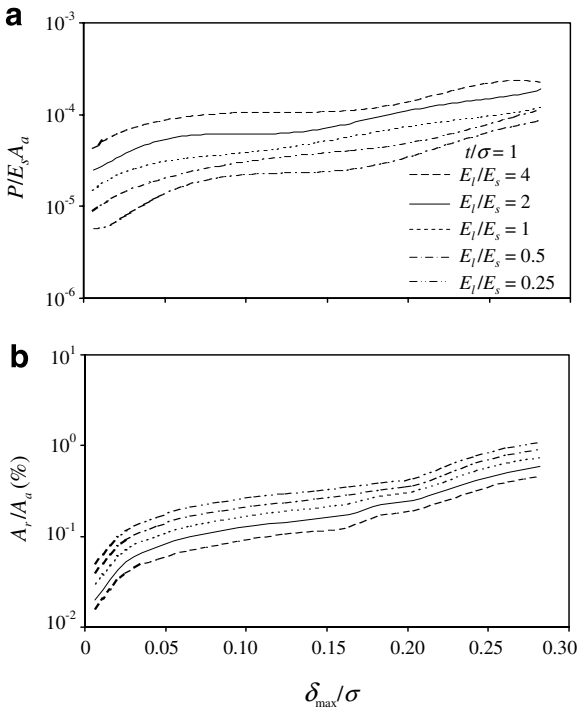

Fig. 11. Effect of layer elastic modulus on (a) contact load and (b) real contact area versus maximum surface interference for a layered elastic medium indented by a rough surface ($t/\sigma = 1$; $D = 1.44$).

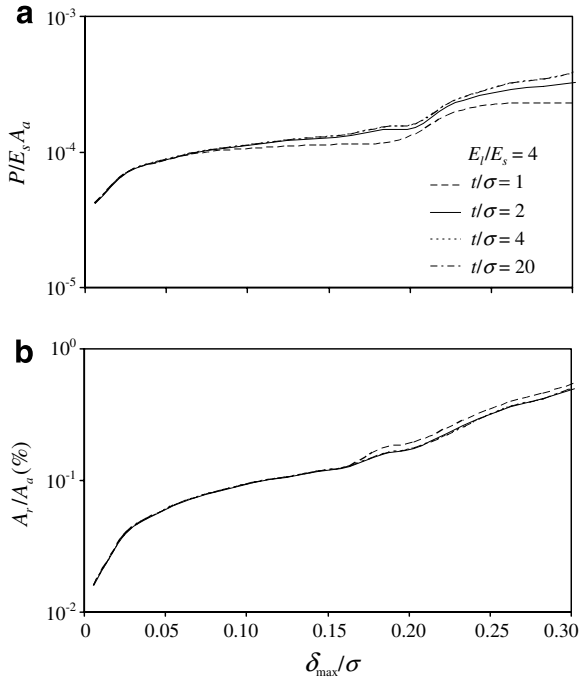

Fig. 12. Effect of layer thickness on (a) contact load and (b) real contact area versus maximum surface interference for a layered elastic medium indented by a rough surface ($E_l/E_s = 4$; $D = 1.44$).

with the increase of E_l/E_s. This is attributed to the enhancement of the stiffness of the layered medium in the presence of a stiff layer.

To illustrate the effect of the layer thickness on the contact load and the real contact area, results for $t/\sigma = 1$, 2, 4, and 20, $E_l/E_s = 4$, and $D = 1.44$ (i.e., fixed σ) are contrasted in Fig. 12. It can be seen that the effect of the layer thickness is negligible for small values of δ_{max}/σ (i.e., low contact load). The results indicate that for a stiff layer ($E_l/E_s = 4$) and a large surface interference, the tendency is for the contact load to increase and the contact area to decrease with increasing layer thickness. This is because the effect of the stiff layer on the contact load and the contact area becomes more pronounced with the increase of the surface interference and the layer thickness. For $\delta_{max}/\sigma < 0.3$, there is no discernible difference between the results for $t/\sigma = 4$ and 20.

4.3. Contact stresses

Accurate estimation of the contact stresses is essential for the analysis of the mechanisms controlling fracture, fatigue, and wear. The effects of the material properties and the layer thickness on the contact stresses due to normal loading are presented first, followed by stress results for the simultaneous application of normal and tangential contact loading.

Fig. 13 shows that the maximum von Mises equivalent stress σ_M^{max} in the layer and the substrate intensifies with the increase of δ_{max}/σ and/or E_l/E_s. This is expected because higher values of δ_{max}/σ and E_l/E_s yield higher contact loads (Fig. 11(a)). For fixed δ_{max}/σ, initial yielding in the substrate is less likely in the presence of a compliant layer (Fig. 13(b)). This is because the compliant layer can store more elastic energy and thus relax the stresses in the substrate. In the case of a stiff layer, stress concentration at the interface due to the large elastic modulus mismatch enhances the propensity for yielding. For $\delta_{max}/\sigma < 0.2$, σ_M^{max} exhibits insignificant variation because the effect of the substrate compliance is secondary. Results (not shown here for brevity) revealed that σ_M^{max} is more likely to occur at or close to the surface for $E_l/E_s = 4$ and in the layer or at the layer/substrate interface for $E_l/E_s = 0.25$. Also the location of σ_M^{max} shifted from the surface to the interface with the

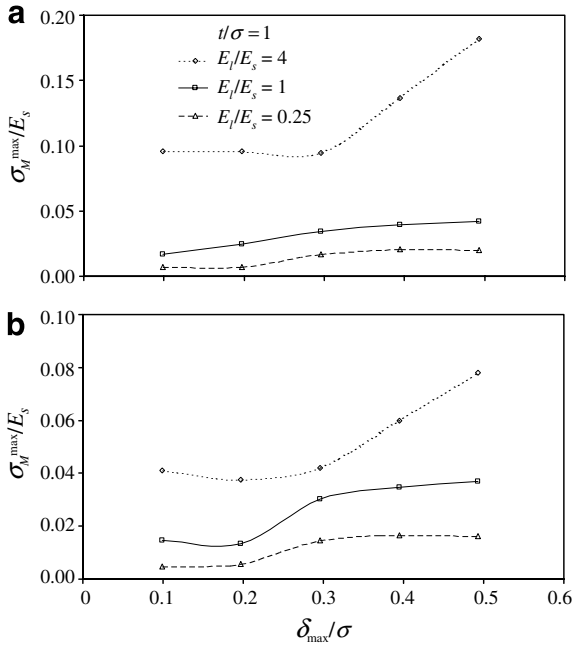

Fig. 13. Maximum von Mises equivalent stress in (a) the layer and (b) the substrate of a layered elastic medium indented by a rough surface ($t/\sigma = 1$; $D = 1.44$) versus maximum surface interference.

increase of δ_{max}/σ, suggesting that low contact loads promote surface yielding, while high contact loads promote yielding at the layer/substrate interface.

Fig. 14 shows σ_M^{max} in the layer and the substrate as a function of δ_{max}/σ for different values of t/σ ($D = 1.44$) and $E_l/E_s = 4$. As expected, σ_M^{max} increases with δ_{max}/σ. The marginal differences between the values of σ_M^{max} in

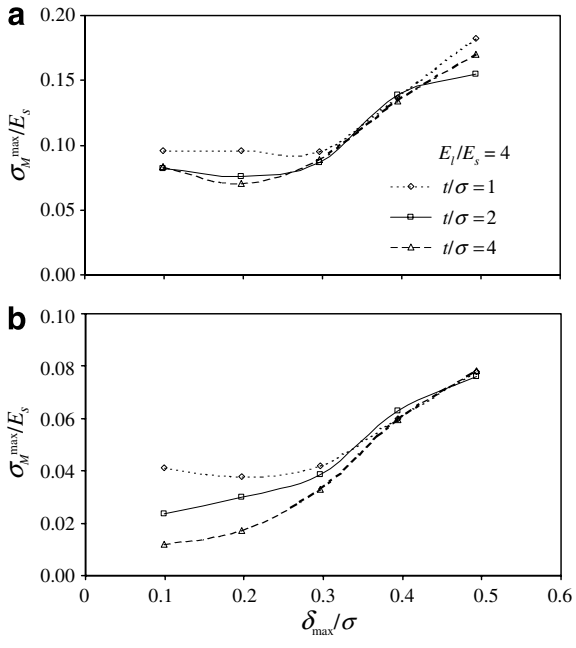

Fig. 14. Maximum von Mises equivalent stress in (a) the layer and (b) the substrate of a layered elastic medium indented by a rough surface ($E_l/E_s = 4$; $t/\sigma = 1$, 2, and 4; $D = 1.44$) versus maximum surface interference.

the layer for $t/\sigma = 2$ and 4 are attributed to the very small differences in the contact load and contact area (Fig. 12). However, Fig. 14(b) shows a strong dependence of σ_M^{max} in the substrate on t/σ for $\delta_{max}/\sigma < 0.3$. The increase of σ_M^{max} in the substrate with deceasing t/σ is attributed to the intensification of the stress field in the substrate due to the decrease of the thickness of the stiff layer. A comparison of Figs. 13 and 14 indicates an overall stronger effect of the layer elastic modulus on σ_M^{max} than the layer thickness.

Fig. 15(a) shows the variation of σ_M^{max} in the layer and the substrate with E_l/E_s for $t/\sigma = 0.23$ and $\delta_{max}/\sigma = 0.25$ ($D = 1.44$). Stiffening of the layer intensified significantly σ_M^{max} in the layer; however, the effect on the σ_M^{max} stress arising in the substrate was less pronounced. A constant σ_M^{max} developed in the substrate for $E_l/E_s \geqslant 3$. Fig. 15(b) shows the variation of σ_M^{max} in the layer and the substrate with t/σ for $\delta_{max}/\sigma = 0.25$ ($D = 1.34$). The increase of t/σ resulted in the decrease of σ_M^{max} in the substrate to a much lower steady-state value. This implies a negligible effect of the layer thickness on σ_M^{max} in the substrate for a relatively thick and stiff layer. The results shown in Fig. 15 indicate the existence of thresholds of E_l/E_s and t/σ above which the layer is most effective in relaxing the stresses in the substrate.

Fig. 16 shows pressure distributions at asperity contacts and contours of subsurface von Mises equivalent stress for $E_l/E_s = 4$, 1, and 0.25, $t/\sigma = 0.23$, and $\delta_{max}/\sigma = 0.25$ ($D = 1.34$). Corresponding segments of the rough surface are also shown above the contact pressure distributions. A comparison of the contact pressure profiles shown in Figs. 16(a)–(c) demonstrates that the stiffer layer produced much higher pressure peaks and smaller contact areas. This is expected because, for a given value of δ_{max}/σ, the contact load increases with E_l/E_s (Fig. 11). For $E_l/E_s = 4$ and 0.25, the contact interface comprised four and five asperity contacts, respectively. The stress contours show a strong dependence of the subsurface stresses on the elastic modulus of the layer. The stress contours for $E_l/E_s = 4$ are essentially confined within the layer and exhibit significant discontinuities at the layer/substrate interface. The increase of σ_M with E_l/E_s is due to the increase of the contact pressure. It is noted that p^{max} and σ_M^{max} always occur at the sharper asperity contact. For $E_l/E_s = 0.25$, the position of σ_M^{max} shifted from the surface to the layer/substrate interface as a result of the increase of the asperity contact area.

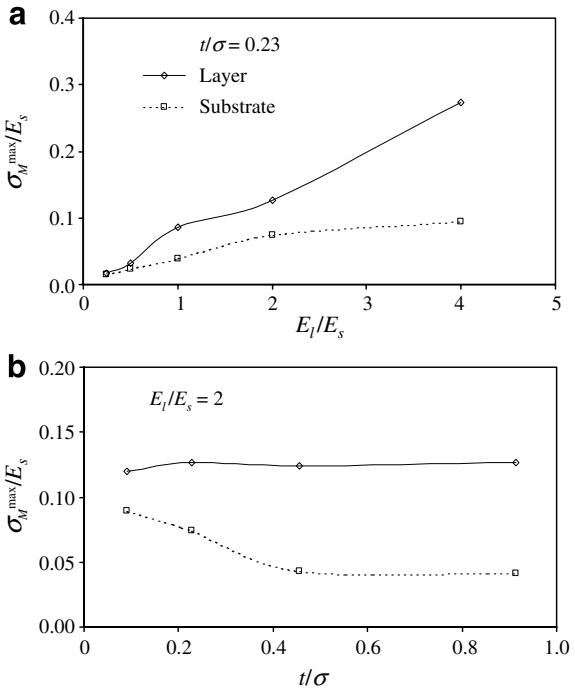

Fig. 15. Effects of (a) layer elastic modulus and (b) layer thickness on the maximum von Mises equivalent stress in a layered elastic medium indented by a rough surface ($t/\sigma = 0.23$; $\delta_{max}/\sigma = 0.25$; $D = 1.34$).

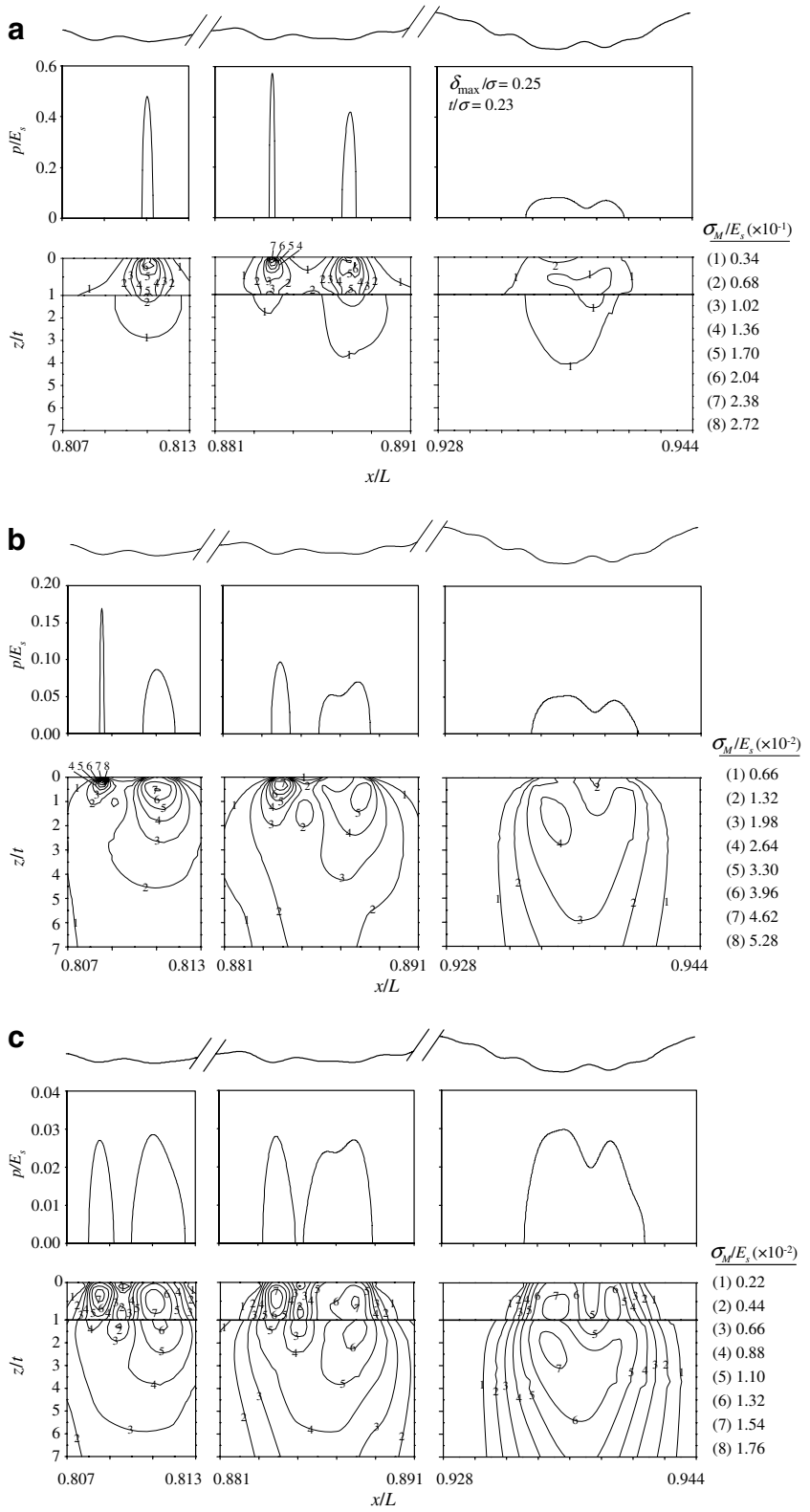

Fig. 16. Pressure distributions at asperity contacts and corresponding contours of von Mises equivalent stress in a layered elastic medium indented by a rough surface ($t/\sigma = 0.23$; $\delta_{max}/\sigma = 0.25$; $D = 1.34$): (a) $E_l/E_s = 4$, (b) $E_l/E_s = 1$, and (c) $E_l/E_s = 0.25$.

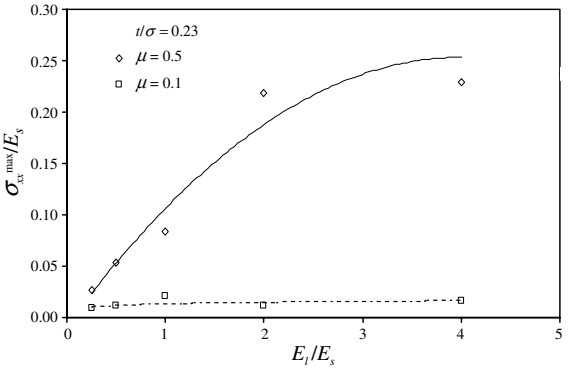

Fig. 17. Effect of layer elastic modulus on maximum tensile stress at the surface of a layered elastic medium due to sliding against a rough surface ($t/\sigma = 0.23$; $\delta_{max}/\sigma = 0.25$; $D = 1.34$; $\mu = 0.5$, 0.1).

To evaluate the effect of friction on the propensity for surface cracking, the maximum tensile stress σ_{xx}^{max} at the layer surface was plotted in Fig. 17 as a function of E_l/E_s for $t/\sigma = 0.23$, $\delta_{max}/\sigma = 0.25$ ($D = 1.34$), and $\mu = 0.1$ and 0.5. In the low-friction case ($\mu = 0.1$), σ_{xx}^{max} was not affected by variations in E_l/E_s, whereas in the high-friction case ($\mu = 0.5$), σ_{xx}^{max} increased significantly with E_l/E_s. The high value of σ_{xx}^{max} for $E_l/E_s = 4$ and $\mu = 0.5$ indicates a greater likelihood for surface cracking. Fig. 18 shows surface distributions of σ_{xx} and subsurface contour plots of σ_I for $E_l/E_s = 4$, 1, and 0.25, $t/\sigma = 0.23$, $\delta_{max}/\sigma = 0.25$ ($D = 1.34$), and $\mu = 0.5$. Corresponding segments of the rough surface are also shown above the σ_{xx} stress plots. The results reveal a similar trend for different E_l/E_s values, i.e., σ_{xx}^{max} always commences at the trailing edges of the asperity contacts. However, a significantly higher σ_{xx}^{max} stress was produced for $E_l/E_s = 4$. The contours of the first principal stress σ_I (which is the surface tensile σ_{xx} stress in the wake of sliding) show the development of significantly higher tensile stresses in the stiff layer, consistent with the conclusion of an earlier study (Kral and Komvopoulos, 1996). Since σ_I^{max} occurs always at the surface, it may be interpreted that surface cracking would be especially prevalent under sliding conditions conducive to high friction coefficients. This has been demonstrated in the fracture analysis of Bower and Fleck (1994) in which crack initiation occurred at the surface behind the contact region of a sliding indenter where the tensile stress reached a maximum. Moreover, three small regions of high tensile stresses arose at the layer/substrate interface for $E_l/E_s = 4$ (Fig. 18(a)). Hence, it may be inferred that while for a relatively stiff layer crack initiation is likely to occur either at the surface or the layer/substrate interface, in the presence of a compliant layer, crack initiation is more likely to occur at the layer surface.

Delamination at the layer/substrate interface depends on the magnitude of the interfacial shear stress. Fig. 19 shows distributions of the interfacial τ_{xz} stress for $E_l/E_s = 4$, 1, and 0.25, $t/\sigma = 0.23$, $\delta_{max}/\sigma = 0.25$ ($D = 1.34$), and $\mu = 0.5$. The results illustrate a strong dependence of the interfacial shear stress on the elastic modulus of the layer. A comparison of the shear stresses obtained for different values of E_l/E_s indicates an increased likelihood for delamination at the layer/substrate interface in the case of the stiff layer. The existence of several interfacial locations of high τ_{xz} stress suggests that delamination may occur at several locations along the interface. Fig. 20(a) shows the maximum shear stress τ_{xz}^{max} at the interface as a function of E_l/E_s for $t/\sigma = 0.23$, $\delta_{max}/\sigma = 0.25$ ($D = 1.34$), and $\mu = 0.1$ and 0.5. The τ_{xz}^{max} stress increases significantly with the increase of the layer stiffness, reaching a steady-state for $E_l/E_s > 2$. The effect of friction on τ_{xz}^{max} is secondary compared to that of E_l/E_s. This is opposite from the trend for the σ_{xx}^{max} stress (Fig. 17). The significance of the layer thickness on the maximum shear stress at the layer/substrate interface can be interpreted in terms of the results shown in Fig. 20(b). Depending on the coefficient of friction, τ_{xz}^{max} may decrease by a factor of 2–3 with the increase of the layer thickness, reaching a constant value for $t/\sigma > 0.4$. This behavior is expected because the substrate effect diminishes with the increase of the layer thickness. A comparison of the shear stress curves for $\mu = 0.1$ and 0.5 shown in Fig. 20 indicates that the effect of the coefficient of friction on the interfacial τ_{xz}^{max} stress is secondary compared to the effects of the layer thickness and the layer elastic modulus.

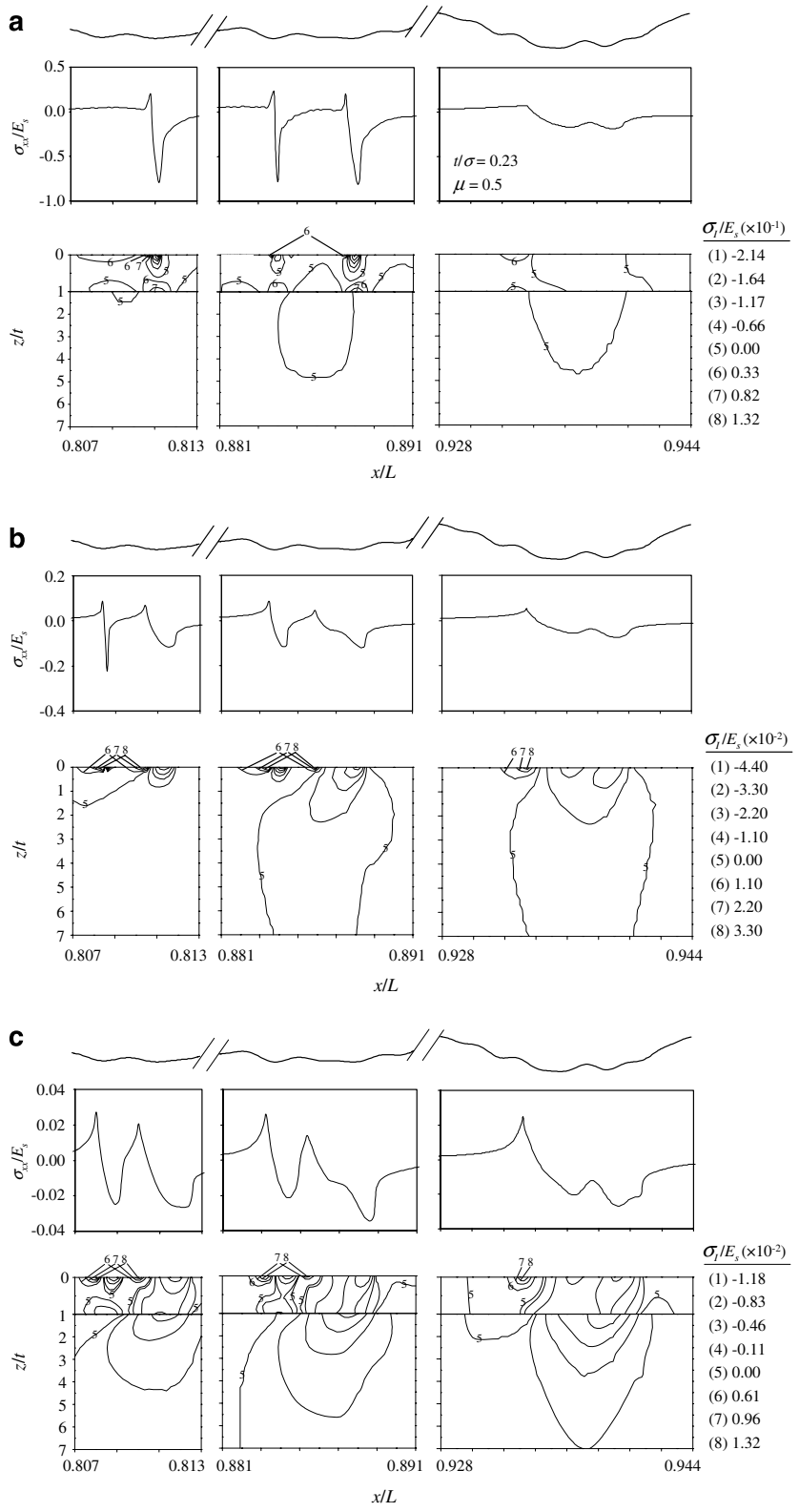

Fig. 18. Surface stress distributions and contours of maximum principal stress in a layered elastic medium due to sliding against a rough surface ($t/\sigma = 0.23$; $\delta_{max}/\sigma = 0.25$; $D = 1.34$): (a) $E_l/E_s = 4$, (b) $E_l/E_s = 1$, and (c) $E_l/E_s = 0.25$.

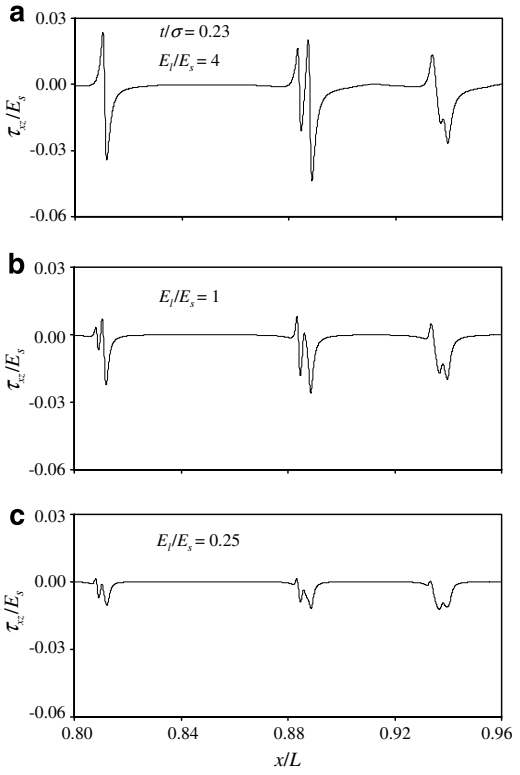

Fig. 19. Shear stress distributions at the interface of a layered elastic medium due to sliding against a rough surface ($t/\sigma = 0.23$; $\delta_{max}/\sigma = 0.25$; $D = 1.34$; $\mu = 0.5$): (a) $E_l/E_s = 4$, (b) $E_l/E_s = 1$, and (c) $E_l/E_s = 0.25$.

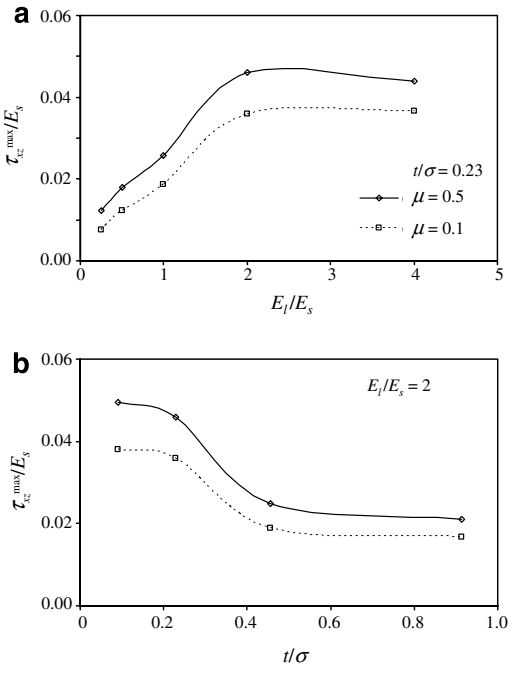

Fig. 20. Effects of (a) layer elastic modulus and (b) layer thickness on the maximum shear stress at the interface of a layered elastic medium due to sliding against a rough surface ($\delta_{max}/\sigma = 0.25$; $D = 1.34$; $\mu = 0.1$, 0.5).

5. Conclusions

A plane-strain analysis was developed for an elastic layered medium in sliding contact with a rough (fractal) surface. The significance of the elastic properties of the layer and the substrate materials, layer thickness, and surface topography on the global deformation behavior was interpreted in the context of results for the contact load and the real contact area. The contact pressure and the local stress fields were analyzed in terms of the coefficient of friction, layer thickness, and elastic properties. Based on the obtained results and discussion, the following main conclusions can be drawn from the present analysis.

(1) A relationship of the mean contact pressure versus representative strain was derived for a layered elastic medium indented by a cylindrical asperity. The real half-contact width of an asperity contact was obtained as a function of the elastic properties of the layered medium, layer thickness, truncated half-contact width, and asperity radius.
(2) Contact pressure profiles and stress distributions were determined for various surface topographies (roughness) by varying the fractal parameter, which controls the contributions of the various frequency components in the surface profile.
(3) Both the contact load and the real contact area increased monotonically with the maximum surface interference. The surface roughness (i.e., fractal parameter) and the elastic modulus of the layer exhibited a dominant effect on the contact load and the real contact area, while the effect of the layer thickness was relatively small. The contact load increased and the contact area decreased with the increase of the layer stiffness. The effect of the layer thickness was negligible for small interferences (or low contact loads) and secondary for relatively large interferences.
(4) The maximum von Mises equivalent stress in the layer and the substrate increased with the maximum interference and the layer elastic modulus. The maximum von Mises stress occurred always at the sharper asperity contacts. A trend for the maximum von Mises stress to develop at or close to the surface was observed with the increase of the layer stiffness. However, for a compliant layer, the maximum von Mises stress occurred either below the surface or at the layer/substrate interface. A strong dependence of the maximum von Mises stress in the substrate on the layer thickness was found for small surface interference.
(5) The maximum tensile stress occurred at the trailing edges of asperity contacts and intensified with the increase of the layer elastic modulus and the coefficient of friction. Significantly higher tensile stresses were obtained for stiff layers than compliant layers. The peak value of the maximum principal stress occurred always at the surface, suggesting a higher probability for crack initiation at the layer surface. However, crack initiation at the layer/substrate interface cannot be precluded in the presence of a stiff layer.
(6) The interfacial shear stress exhibited a strong dependence on the thickness and elastic modulus of the layer. A stiff layer increased the likelihood for interface cracking and delamination at the layer/substrate interface much more than a compliant layer. The effect of the coefficient of friction on the interfacial shear stress was found to be secondary compared to the effects of the thickness and the elastic modulus of the layer.

References

Aleksandrov, V.M., Babeshko, V.A., Kucherov, V.A., 1966. Contact problems for an elastic layer of slight thickness. Journal of Applied Mathematics and Mechanics (PMM) 30, 124–142.

Archard, J.F., 1957. Elastic deformation and the laws of friction. Proceedings of the Royal Society of London A 243, 190–205.

Barber, J.R., 2003. Bounds on the electrical resistance between contacting elastic rough bodies. Proceedings of the Royal Society of London A 459, 53–66.

Bhattacharya, A.K., Nix, W.D., 1988. Analysis of elastic and plastic deformation associated with indentation testing of thin films on substrates. International Journal of Solids and Structures 24, 1287–1298.

Bower, A.F., Fleck, N.A., 1994. Brittle fracture under a sliding line contact. Journal of the Mechanics and Physics of Solids 42, 1375–1396.

Burmister, D.M., 1945. The general theory of stresses and displacements in layered systems. Journal of Applied Physics 16, 89–94.

Bush, A.W., Gibson, R.D., Thomas, T.R., 1975. Elastic contact of a rough surface. Wear 35, 87–111.

Bush, A.W., Gibson, R.D., Keogh, G.P., 1979. Strongly anisotropic rough surfaces. Journal of Lubrication Technology 101, 15–20.
Chang, W.R., Etsion, I., Bogy, D.B., 1987. An elastic–plastic model for the contact of rough surfaces. Journal of Tribology 109, 257–263.
Ciavarella, M., Demelio, G., Barber, J.R., Jang, Y.H., 2000. Linear elastic contact of the Weierstrass profile. Proceedings of the Royal Society of London A 456, 387–405.
Ciavarella, M., Leoci, F., 2006. An assessment of the Greenwood–Williamson and other asperities models, with special reference to electrical conductance. Journal of Tribology 128, 10–17.
Gibson, R.D., 1982. The surface as a random process. In: Thomas, T.R. (Ed.), Rough Surfaces. Longman, London, UK.
Gong, Z.-Q., Komvopoulos, K., 2005. Thermomechanical analysis of semi-infinite solid in sliding contact with a fractal surface. Journal of Tribology 127, 331–342.
Greenwood, J.A., Williamson, J.B.P., 1966. Contact of nominally flat surfaces. Proceedings of the Royal Society of London A 295, 300–319.
Greenwood, J.A., Wu, J.J., 2001. Surface roughness and contact: an apology. Meccanica 36, 617–630.
Gupta, P.K., Walowit, J.A., Finkin, E.F., 1973. Stress distributions in plane strain layered elastic solids subjected to arbitrary boundary loading. Journal of Lubrication Technology 95, 427–433.
Gupta, P.K., Walowit, J.A., 1974. Contact stresses between an elastic cylinder and a layered elastic solid. Journal of Lubrication Technology 96, 250–257.
Hertz, H., 1882. Über die Bierührung fester elastischer körper (On the contact of elastic solids). Journal Reine und Angewandte Mathematik 92, 156–171.
Hyun, S., Pei, L., Molinari, J.-F., Robbins, M.O., 2004. Finite-element analysis of contact between elastic self-affine surfaces. Physical Review E 70, 026117-1–026117-12.
Ioannides, E., Kuijpers, J.C., 1986. Elastic stresses below asperities in lubricated contacts. Journal of Tribology 108, 394–402.
Johnson, K.L., 1985. Contact Mechanics. Cambridge University Press, Cambridge, UK.
King, R.B., 1987. Elastic analysis of some punch problems for a layered medium. International Journal of Solids and Structures 23, 1657–1664.
King, R.B., O'Sullivan, T.C., 1987. Sliding contact stresses in a two-dimensional layered elastic half-space. International Journal of Solids and Structures 23, 581–597.
Kogut, L., Komvopoulos, K., 2003a. Electrical contact resistance theory for conductive rough surfaces. Journal of Applied Physics 94, 3153–3162.
Kogut, L., Komvopoulos, K., 2003b. Analysis of interfacial adhesion based on electrical contact resistance measurements. Journal of Applied Physics 94, 6386–6390.
Kogut, L., Komvopoulos, K., 2004. Electrical contact resistance theory for conductive rough surfaces separated by a thin insulating film. Journal of Applied Physics 95, 576–585.
Komvopoulos, K., 1988. Finite element analysis of a layered elastic solid in normal contact with a rigid surface. Journal of Tribology 110, 477–485.
Komvopoulos, K., 1989. Elastic–plastic finite element analysis of indented layered media. Journal of Tribology 111, 430–439.
Komvopoulos, K., 2000. Head-disk interface contact mechanics for ultrahigh density magnetic recording. Wear 238, 1–11.
Komvopoulos, K., Choi, D.-H., 1992. Elastic finite element analysis of multi-asperity contacts. Journal of Tribology 114, 823–831.
Komvopoulos, K., Yan, W., 1997. A fractal analysis of stiction in microelectromechanical systems. Journal of Tribology 119, 391–400.
Komvopoulos, K., Ye, N., 2001. Three-dimensional contact analysis of elastic–plastic layered media with fractal surface topographies. Journal of Tribology 123, 632–640.
Komvopoulos, K., Ye, N., 2002. Elastic–plastic finite element analysis for the head-disk interface with fractal topography description. Journal of Tribology 124, 775–784.
Kral, E.R., Komvopoulos, K., 1996. Three-dimensional finite element analysis of surface deformation and stresses in an elastic–plastic layered medium subjected to indentation and sliding contact loading. Journal of Applied Mechanics 63, 365–375.
Majumdar, A., Bhushan, B., 1990. Role of fractal geometry in roughness characterization and contact mechanics of surfaces. Journal of Tribology 112, 205–216.
Mandelbrot, B.B., 1983. The Fractal Geometry of Nature. Freeman, New York.
McCool, J.I., 1986. Predicting microfracture in ceramics via a microcontact model. Journal of Tribology 108, 380–386.
Nowell, D., Hills, D.A., 1989. Hertzian contact of ground surfaces. Journal of Tribology 111, 175–179.
Pao, Y.C., Wu, T.-S., Chiu, Y.P., 1971. Bounds on the maximum contact stress of an indented elastic layer. Journal of Applied Mechanics 38, 608–614.
Persson, B.N.J., 2001. Theory of rubber friction and contact mechanics. Journal of Chemical Physics 115, 3840–3861.
Persson, B.N.J., Bucher, F., Chiaia, B., 2002. Elastic contact between randomly rough surfaces: comparison of theory with numerical results. Physical Review B 65, 184106-1–184106-7.
Van der Zwaag, S., Field, J.E., 1982. The effect of thin hard coatings on the Hertzian stress field. Philosophical Magazine A 46, 133–150.
Wang, S., Komvopoulos, K., 1994a. A fractal theory of the interfacial temperature distribution in the slow sliding regime: Part I – Elastic contact and heat transfer analysis. Journal of Tribology 116, 812–823.
Wang, S., Komvopoulos, K., 1994b. A fractal theory of the interfacial temperature distribution in the slow sliding regime: Part II – Multiple domains, elastoplastic contacts and applications. Journal of Tribology 116, 824–832.
Yan, W., Komvopoulos, K., 1998. Contact analysis of elastic–plastic fractal surfaces. Journal of Applied Physics 84, 3617–3624.